Optical emission spectroscopic study of plasma plumes generated by IR CO_2 pulsed laser on carbon targets

2008 J. Phys. D: Appl. Phys. 41 105201

(http://iopscience.iop.org/0022-3727/41/10/105201)

J. Phys. D: Appl. Phys. **41** (2008) 105201 (13pp) doi:10.1088/0022-3727/41/10/105201

Optical emission spectroscopic study of plasma plumes generated by IR CO_2 pulsed laser on carbon targets

J J Camacho[1], L Díaz[2], M Santos[2], D Reyman[1] and J M L Poyato[1]

[1] Departamento de Química-Física Aplicada, Facultad de Ciencias, Universidad Autónoma de Madrid, Cantoblanco, 28049-Madrid, Spain
[2] Instituto de Estructura de la Materia, CFMAC, CSIC, Serrano 121, 28006-Madrid, Spain

E-mail: j.j.camacho@uam.es

Received 11 December 2007, in final form 28 February 2008
Published 8 April 2008
Online at stacks.iop.org/JPhysD/41/105201

Abstract

Optical emission spectroscopy studies, in the spectral range ultraviolet–visible–near infrared (UV–Vis–NIR), were performed to investigate thermal and dynamical properties of a plume produced by laser ablation of a graphite target. Ablation is carried out using a high-power IR CO_2 pulsed laser at $\lambda = 9.621\ \mu$m, power density ranging from 0.22 to 5.36 GW cm^{-2} and air pressures around 4 Pa. The strong emission observed in the plasma region is mainly due to electronic relaxation of excited C, ionic fragments C^+, C^{2+} and C^{3+} and molecular features of $C_2(d\,^3\Pi_g–a\,^3\Pi_u$; Swan band system). The medium-weak emission is mainly due to excited atomic N, H, O, ionic fragment C^{4+} and molecular features of $C_2(E\,^1\Sigma_g^+–A\,^1\Pi_u$; Freymark system), $C_2(D\,^1\Sigma_u^+–X\,^1\Sigma_g^+$; Mulliken system), $CN(D\,^2\Pi–A\,^2\Pi)$, $C_2(e\,^3\Pi_g–a\,^3\Pi_u$; Fox–Herzberg system), $C_2(C\,^1\Pi_g–A\,^1\Pi_u$; Deslandres–d'Azambuja system), $OH(A\,^2\Sigma^+–X\,^2\Pi)$, $CH(C\,^2\Sigma^+–X\,^2\Pi)$, $NH(A\,^3\Pi–X\,^3\Sigma^-)$, $CN(B\,^2\Sigma^+–X\,^2\Sigma^+$; violet system), $CH(B\,^2\Sigma^+–X\,^2\Pi)$, $CH(A\,^2\Delta–X\,^2\Pi)$, $C_2(A\,^1\Pi_u–X\,^1\Sigma_g^+$; Phillips system) and $CN(A\,^2\Pi–X\,^2\Sigma^+$; red system). An excitation temperature $T_{exc} = 23\,000 \pm 1900$ K and electron densities in the range (0.6–5.6) $\times\ 10^{16}$ cm^{-3} were estimated by means of C^+ ionic lines. The characteristics of the spectral emission intensities from different species have been investigated as functions of the ambient pressure and laser irradiance. Estimates of vibrational temperatures of C_2 and CN electronically excited species under various laser irradiance conditions are made.

(Some figures in this article are in colour only in the electronic version)

1. Introduction

Carbon materials such as graphite, diamond, fullerenes, carbon nanofibres and carbon nanotubes are promising as electronics components, scanning probes, hydrogen storage and field emitters. So far, the growth of diamond, carbon nanofibres and carbon nanotubes has been performed mostly through chemical vapour deposition (CVD), arc discharge and laser ablation methods [1–6]. Pulsed laser ablation (PLA) provides a means of depositing thin coatings, of a wide range of target materials, on a wide range of substrates, at room temperature. Diamond-like carbon (DLC) thin films have attracted a considerable amount of scientific interest in the field of electronic research due to their outstanding properties, such as high hardness, chemical inertness, high thermal conductivity, high electrical resistivity and optical transparency from UV to IR [7]. For the production of high-quality DLC films through PLA, it is necessary to understand the formation of atomic and molecular species and their dependence on various parameters such as the laser power density, pressure of the boundary ambient atmosphere, concentration of the species at different distances from the target and so forth. Despite its versatility and wide applicability, however, many aspects of the detailed chemical physics underlying the ablation process are still far from completely understood. The process is often envisaged as a

sequence of steps, initiated by the laser radiation interacting with the solid target, absorption of energy and localized heating of the surface and subsequent material evaporation. The properties and composition of the resulting ablation plume may evolve, both as a result of collisions between particles in the plume and through plume–laser radiation interactions. The laser–target interactions will be sensitively dependent both on the nature and condition of the target material and on the laser pulse parameters. Subsequent laser–plume interactions will also be dependent on the properties of the laser radiation, while the evolution and propagation of the plume will also be sensitive to collisions and thus to the quality of the vacuum under which the ablation is conducted and/or the presence of any background gas. Obviously, the ultimate composition and velocity distribution of the ejected material is likely to be reflected in the detailed characteristics of any deposited film.

Optical emission spectroscopy (OES) is a powerful tool to get information on the laser-ablated species. For laser ablation of carbon, OES studies in different atmospheres are reported and these studies have yielded many interesting results [8–31]. Detailed studies of laser-induced breakdown spectroscopy on N_2 and Si_3H_8 in the gas phase have been recently made in our laboratory [32, 33].

In this work, OES has been used to investigate thermal and dynamical properties of a plume produced by laser ablation of a graphite target at air pressures around 4 Pa. Ablation is performed using a high-power IR CO_2 pulsed laser. The emission generated by the plasma in the spectral region 200–1100 nm is due to electronic relaxation of excited C, N, H, O, ionic fragments C^+, C^{2+}, C^{3+}, C^{4+}, and molecular features of $C_2(E\,^1\Sigma_g^+–A\,^1\Pi_u$; Freymark system), $C_2(D\,^1\Sigma_u^+–X\,^1\Sigma_g^+$; Mulliken system), $CN(D\,^2\Pi–A\,^2\Pi)$, $C_2(e\,^3\Pi_g–a\,^3\Pi_u$; Fox–Herzberg system), $C_2(C\,^1\Pi_g–A\,^1\Pi_u$; Deslandres–d'Azambuja system), $OH(A\,^2\Sigma^+–X\,^2\Pi)$, $CH(C\,^2\Sigma^+–X\,^2\Pi)$, $NH(A\,^3\Pi–X\,^3\Sigma^-)$, $CN(B\,^2\Sigma^+–X\,^2\Sigma^+$; violet system), $C_2(d\,^3\Pi_g–a\,^3\Pi_u$; Swan band system), $CH(B\,^2\Sigma^+–X\,^2\Pi)$, $CH(A\,^2\Delta–X\,^2\Pi)$, $C_2(A\,^1\Pi_u–X\,^1\Sigma_g^+$; Phillips system) and $CN(A\,^2\Pi–X\,^2\Sigma^+$; red system). As far as we know, a spectrum so rich in atomic lines belonging to ionized species and molecular features has not been previously observed in similar experiments. The excitation temperature and electron densities were obtained from C^+ ionic lines. We have also studied here the spectral emission intensities from different species as functions of the ambient pressure and laser irradiance. Estimates of vibrational temperatures of C_2 and CN electronically excited species under various laser irradiance conditions are reported.

2. Experimental

2.1. Experimental details

The schematic diagram of the experimental setup is shown in figure 1. A transverse excitation atmospheric (TEA) CO_2 laser (Lumonics model K-103) operating on an 8 : 8 : 84 mixture of $CO_2 : N_2 : He$, respectively, was employed to ablate a graphite target. The laser is equipped with frontal Ge multimode optics (35% reflectivity) and a rear diffraction grating with 135 lines mm^{-1} blazed at 10.6 μm. The CO_2 laser irradiation

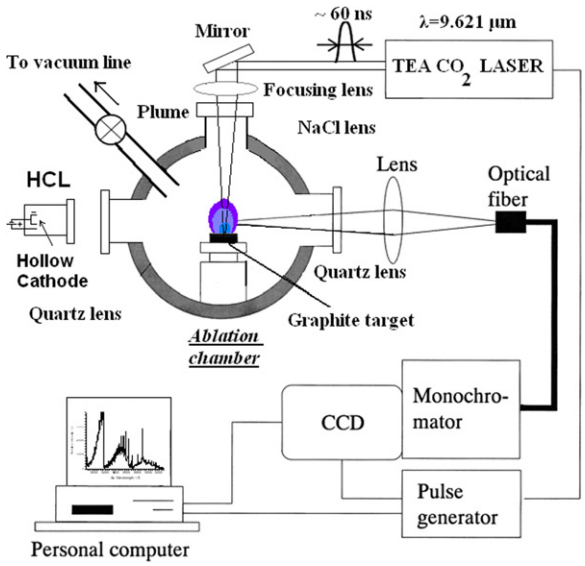

Figure 1. Schematic diagram of the experimental setup for PLA diagnostics.

of the carbon target was carried out using the 9P(28) line at $\lambda = 9.621\,\mu$m. This wavelength was checked with a 16-A spectrum analyser (Optical Eng. Co.). The pulse temporal profile is monitored with a photon drag detector (Rofin Sinar 7415). The temporal shape of the TEA-CO_2 laser pulse consisted of a prominent spike of a full width at half maximum (FWHM) of 64 ns carrying ~90% of the laser energy, followed by a long lasting tail of lower energy and about 3 μs duration. The pulsed CO_2 laser beam was perpendicularly focused with a NaCl lens of 24 cm focal length onto the target surface. The CO_2 laser energy was measured in front of the lens with a Lumonics 20D pyroelectric detector through a Tektronix TDS 540 digital oscilloscope. The focused radius of the laser beam was measured at the target position with a pyroelectric array Delta Development Mark IV. The laser intensity (power density or irradiance) on the target surface ranges from 0.22 to 5.36 GW cm^{-2}. The high purity graphite target (~99.99%) was placed in a low-vacuum cell equipped with a NaCl window for the laser beam and two quartz windows for optical access. The graphite target is initially at ambient temperature (298 K) and it is not water-cooled. The cell was evacuated with the aid of a rotary pump, to a base pressure of 4 Pa that was measured by a mechanical gauge. Optical emission from the plume was imaged by a collecting optical system onto the entrance slit of different monochromators. All the experimental measurements were taken at a constant distance of 1.5 cm from the target surface along the plasma expansion direction and 10 cm in the direction perpendicular to the plasma symmetry axis. In the low-resolution experiments the optical emission from the plume was collected and imaged onto an optical fibre using a quartz lens of 5 cm focal length. The quartz lens causes a slight chromatic aberration for OES measurements, although the geometric efficiency is barely affected. Two spectrometers were used: 1/8 m Oriel spectrometer (10 and 25 μm slits) with two different gratings (1200 and 2400 grooves mm^{-1}) in the spectral region 2000–11000 Å at a resolution of ~1.3 Å

Table 1. Laser parameters for the present experiments.

Energy E_W (mJ)	Power P_W (MW)	Intensity I_W (GW cm^{-2})	Fluence Φ_W (J cm^{-2})	Photon flux, F_{ph} (photon cm^{-2} s^{-1})	Electric field F_E (MV cm^{-1})
2685	42.1	5.36	342	2.60×10^{29}	1.50
2256	35.4	4.50	287	2.18×10^{29}	1.37
1732	27.1	3.46	220	1.67×10^{29}	1.20
1209	19.0	2.41	154	1.17×10^{29}	1.01
503	7.88	1.00	64.0	4.86×10^{28}	0.649
324	5.08	0.648	41.3	3.14×10^{28}	0.521
273	4.27	0.544	34.7	2.64×10^{28}	0.478
242	3.79	0.483	30.8	2.34×10^{28}	0.450
203	3.19	0.406	25.9	1.97×10^{28}	0.413
171	2.68	0.341	21.8	1.65×10^{28}	0.378
149	2.33	0.297	19.0	1.44×10^{28}	0.353
131	2.08	0.262	16.7	1.26×10^{28}	0.331
110	1.73	0.220	14.0	1.07×10^{28}	0.304

in first-order (1200 grooves mm^{-1} grating) and an ISA Jobin Yvon Spex (Model HR320) 0.32 m equipped with a plane holographic grating (2400 grooves mm^{-1}) in the spectral region 2000–7500 Å at a resolution of ∼0.12 Å in first order. The detector is an Andor DU420-OE (open electrode) CCD (charge-coupled device) camera (1024 × 256 matrix of $26 \times 26\,\mu m^2$ individual pixels) with thermoelectric cooling working at −30 °C. The low noise level of the CCD allows long integration times and therefore the detection of very low emission intensities. Many of the spectra were obtained with 5 s integration time over the entire luminous plasma event. The intensity response of the detection system was calibrated with a standard (Osram No 6438, 6.6-A, 200-W) halogen lamp and a Hg/Ar pencil lamp. Several (Cu/Ne, Fe/Ne and Cr/Ar) hollow cathode lamps (HCLs) were used for the spectral wavelength calibration of the spectrometers.

2.2. *Laser parameters for the present experiments*

The laser peak power or radiant pulse energy per time P_W (W) is given by

$$P_W = E_W/\tau_{FWHM}, \tag{1}$$

E_W (J) being the pulse energy and τ_{FWHM} (s) the pulse duration at the FWHM. The laser peak intensity (power density or irradiance) I_W (W cm^{-2}), fluence Φ_W on target (J cm^{-2}), the photon flux F_{ph} (photon cm^{-2} s^{-1}) and electric field F_E (V cm^{-1}) are given by

$$I_W = P_W/\pi r^2, \tag{2}$$

$$\Phi_W = E_W/\pi r^2, \tag{3}$$

$$F_{ph} = P_W\lambda/\pi r^2 hc, \tag{4}$$

$$F_E = \sqrt{4P_W/r^2 c}, \tag{5}$$

where πr^2 is the focal spot area (cm^2) and λ is the laser wavelength. For the present experiments, the graphite ablation is performed using a high-power IR CO_2 pulsed laser at $\lambda = 9.621\,\mu$m, $\tau_{FWHM} = 64$ ns and the focused-spot area was 7.5×10^{-3} cm^2. For the different pulse laser energies measured in this work, the calculated laser peak power (equation (1)), intensity (equation (2)), fluence (equation (3)), photon flux (equation (4)) and electric field (equation (5)) are tabulated in table 1.

3. Results and discussion

3.1. *Identification of the chemical species in the PLA plasma plume*

In the scanned spectral region, from UV to NIR, OES reproduce particular emission of carbon plasmas in a low-vacuum air atmosphere ($P_{air} = 4$ Pa). Typical time-integrated and spectral-resolved low-resolution (1/8 m Oriel spectrometer to a resolution of ∼1.3 Å) OES from PLA of graphite is shown in figures 2(*a*)–(*f*). In the recording of the spectra of figures 2(*c*)–(*f*) a cutoff filter was used in order to suppress high diffraction orders. These plasma plumes were generated by the CO_2 laser intensity of 1.00 GW cm^{-2}. In general, the spectra of the PLA plume are dominated by emission of strong electronic relaxation of excited atomic C, ionic fragments C^+, C^{2+} and C^{3+} and molecular features of $C_2(d\,^3\Pi_g$–$a\,^3\Pi_u$; triplet Swan band system). The medium-weak emission is mainly due to excited atomic N, H, O, ionic fragment C^{4+} and molecular features of $C_2(E\,^1\Sigma_g^+$–$A\,^1\Pi_u$; Freymark system), $C_2(D\,^1\Sigma_u^+$–$X\,^1\Sigma_u^+$; Mulliken system), $CN(D\,^2\Pi$–$A\,^2\Pi)$, $C_2(e\,^3\Pi_g$–$a\,^3\Pi_u$; Fox–Herzberg system), $C_2(C\,^1\Pi_g$–$A\,^1\Pi_u$; Deslandres–d'Azambuja system), $OH(A\,^2\Sigma^+$–$X\,^2\Pi)$, $CH(C\,^2\Sigma^+$–$X\,^2\Pi)$, $NH(A\,^3\Pi$–$X\,^3\Sigma^-)$, $CN(B\,^2\Sigma^+$–$X\,^2\Sigma^+$; violet system), $CH(B\,^2\Sigma^+$–$X\,^2\Pi)$, $CH(A\,^2\Delta$–$X\,^2\Pi)$, $C_2(A\,^1\Pi_u$–$X\,^1\Sigma_g^+$; Phillips system) and $CN(A\,^2\Pi$–$X\,^2\Sigma^+$; red system).

In the spectrum of figure 2(*a*) in the 1920–3480 Å region, very strong atomic C, C^+, C^{2+} and C^{3+} lines dominate, but also weak C^{4+} and molecular bands of $C_2(E$–A; $\Delta v = v' - v'' = +2, +1, 0, -1$ sequence from 200 to 222 nm), $C_2(D$–X; $\Delta v = 0$ sequence near 231.4 nm), $CN(D$–A; in the spectral range 223–260 nm), $C_2(e$–a; in the spectral range 240–290 nm), $CN(B$–X; $\Delta v = 3$ sequence from 306 to 326 nm), $OH(A$–X; $\Delta v = 0$ sequence from 306 to 318 nm), $CH(C$–X; $\Delta v = 0$ sequence from 314 to 317 nm), $NH(A$–X; $\Delta v = 0$ sequence

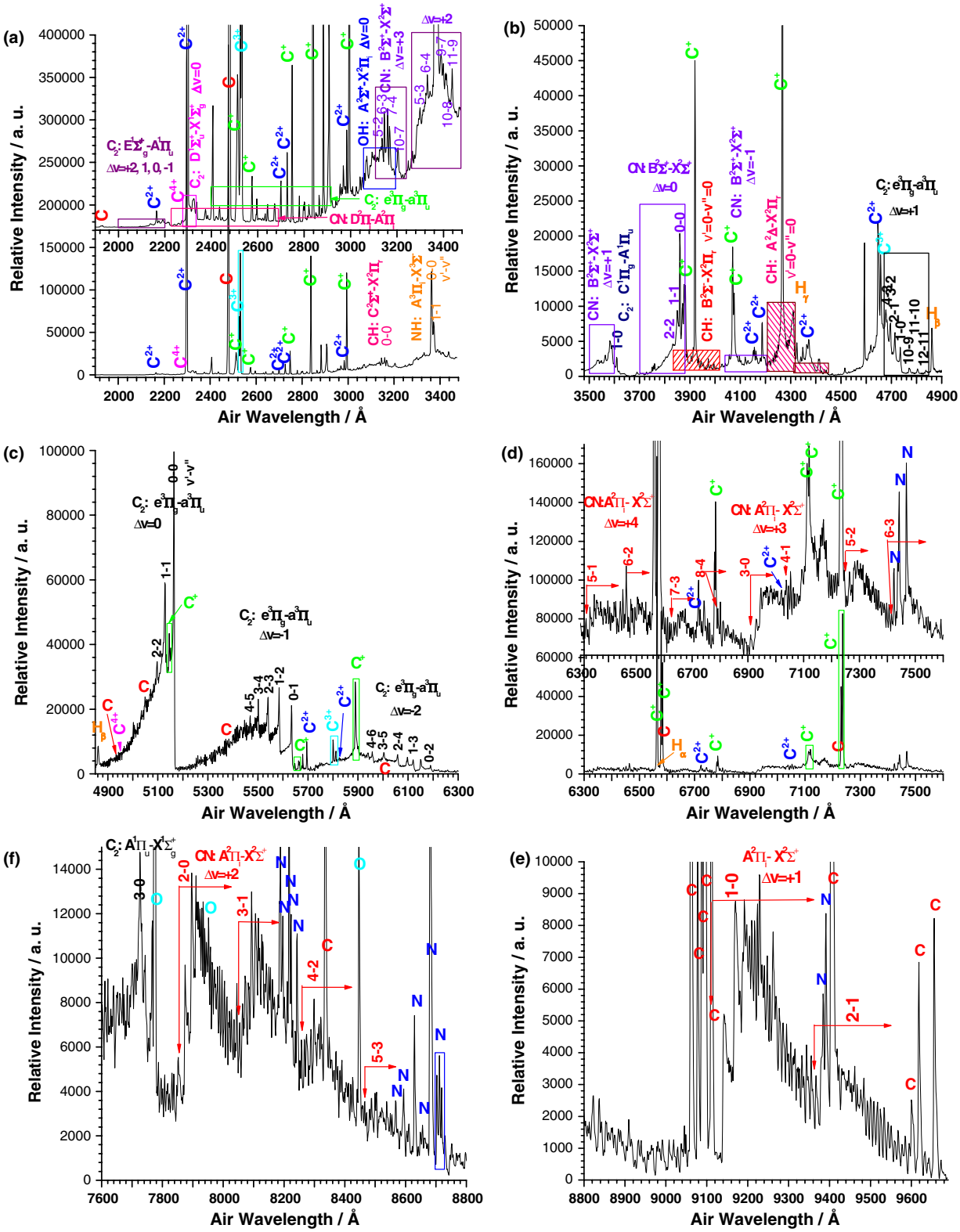

Figure 2. Low-resolution PLA of carbon emission spectrum observed in the 1920–9680 Å region at an air pressure of 4 Pa, excited by the 10P(20) line at 944.20 cm^{-1} of the CO_2 laser, and assignment of the atomic lines of C, C^+, C^{2+}, C^{3+}, C^{4+}, N, O and molecular bands of $C_2(E\,^1\Sigma_g^+–A\,^1\Pi_u$; Freymark system), $C_2(D\,^1\Sigma_u^+–X\,^1\Sigma_u^+$; Mulliken system), $C_2(e\,^3\Pi_g–a\,^3\Pi_u$; Fox–Herzberg system), CN($D\,^2\Pi_i–A\,^2\Pi_i$), OH($A\,^2\Sigma^+–X\,^2\Pi$), CH($C\,^2\Sigma^+–X\,^2\Pi$), CN($B\,^2\Sigma^+–X\,^2\Sigma^+$; violet system), NH($A\,^3\Pi–X\,^3\Sigma^-$), $C_2(C\,^1\Pi_g–A\,^1\Pi_u$; Deslandres–d'Azambuja system), $C_2(d\,^3\Pi_g–a\,^3\Pi_u$; Swan band system), CH($B\,^2\Sigma^+–X\,^2\Pi$), CH($A\,^2\Delta–X\,^2\Pi$), $C_2(A\,^1\Pi_u–X\,^1\Sigma_g^+$; Phillips system) and CN($A\,^2\Pi–X\,^2\Sigma^+$; red system).

near 336 nm) and CN(B–X; $\Delta v = 2$ sequence from 326 to 348 nm) are observed. In this spectrum the predominant emitting species are the C^{2+} $2p^2\,{}^1D_2 \rightarrow 2s2p\,{}^1P^o_1$ atomic line at 2296.87 Å, C $2p({}^2P_0)3s\,{}^1P^o_1 \rightarrow 2p^2\,{}^1S_0$ atomic line at 2478.56 Å, two lines of C^{3+} at 2524.41 and 2529.98 Å, several lines of C^+ at 2836.71 and 2992.62 Å and the $v' = 0 - v'' = 0$ band of NH(A–X) at 3360 Å. In the spectrum of figure 2(b), the predominant emitting species are C^+ (doublet $2s^24s\,{}^2S_{1/2} \rightarrow 2s^23p\,{}^2P^o_{1/2,3/2}$ at 3918.98 and 3920.69 Å, respectively, and multiplet $2s^24f\,{}^2F^o_{J'} \rightarrow 2s^23d\,{}^2D_{J''}$ around 4267 Å), and the molecular bands of CN(B–X; $\Delta v = 0$ sequence). Many medium intensity atomic lines of C^+, C^{2+} and C^{3+}, weak hydrogen lines of the Balmer series (H_β, H_γ, etc), and several molecular bands of CN, C_2 and CH are also present. In the spectrum of figure 2(c), the predominant emitting species are C^+ and C_2 (molecular bands: e–a; $\Delta v = 0$, -1 and -2 sequences from 480 to 630 nm). Many weak lines of C, C^+, C^{2+} and C^{3+} are also present. In the spectrum of figure 2(d), the most intense lines are the doublet structure of C^+ $2s^23p\,{}^2P^o_{3/2,1/2} \rightarrow 2s^23s\,{}^2S_{1/2}$ at 6578.05 and 6582.88 Å, respectively, C $2s^22p({}^2P_0)4d\,{}^1P^o_1 \rightarrow 2s^22p({}^2P_o)3p\,{}^1P_1$ atomic line at 6587.61 Å, C^+ $2s^23d\,{}^2D_{3/2} \rightarrow 2s^23p\,{}^2P^o_{1/2}$ at 7231.32 Å and C^+ $2s^23d\,{}^2D_{5/2} \rightarrow 2s^23p\,{}^2P^o_{3/2}$ at 7236.42 Å. Also many weak lines of C, C^+, C^{2+}, H_α, N, and several bands v'–v'' (5–1, 6–2, 7–3, 8–4, 3–0, 4–1, 5–2 and 6–3) corresponding to CN(A–X) are also present. The spectrum of figure 2(e) shows the emission of many atomic lines of C, O and N, the 3–0 band of C_2(A–X) and several bands (2–0, 3–1, 4–2 and 5–3) of CN(A–X). Finally, in the spectrum of figure 2(f), the emission of many atomic lines of C and N and mainly the 1–0 and 2–1 bands of CN(A–X) can be appreciated.

For the assignment of the atomic lines of C, C^+, C^{2+}, C^{3+}, C^{4+}, H, N and O we used the information tabulated in NIST Atomic Spectral Database [34]. The observed emission molecular bands are identified using the spectroscopic information available in [35–39]. Moreover, these molecular bands were compared with the spectra obtained in our laboratory by conventional sources (free-burning carbon arc, propane–butane/air flame and acetylene/oxygen flame). As an example, figure 3 shows several time-resolved OES at low resolution from (a) PLA of carbon (air pressure of 4 Pa and CO_2 laser power density $I_W = 1.00\,\mathrm{GW\,cm^{-2}}$); ($b$) acetylene/oxygen flame; (c) propane–butane/air flame; (d) free-burning carbon arc. In the acetylene/oxygen flame around 405 nm, several bands of the C_3($\tilde{A}\,{}^1\Pi_u$–$\tilde{X}\,{}^1\Sigma^+_g$) comet head group are observed which were not detected in the PLA of carbon. As shown in figure 3, ionic carbon lines C^+, C^{2+}, C^{3+} and C^{4+} cannot be observed in flames (figures 3(b) and (c)) or carbon electric arcs (figure 3(d)).

In order to get more insight into PLA of graphite and to obtain an unambiguous assignment of the emission lines and molecular bands, we have scanned the corresponding wavelength regions with higher resolution (~0.12 Å in first order). The spectra have been obtained with 24 successive exposures on the CCD camera in the spectral region 200–750 nm by a ISA Jobin Yvon Spex 0.32 m spectrometer. As examples, figures 4(a)–(f) show several spectra recorded in the PLA of carbon experiment at high resolution. These

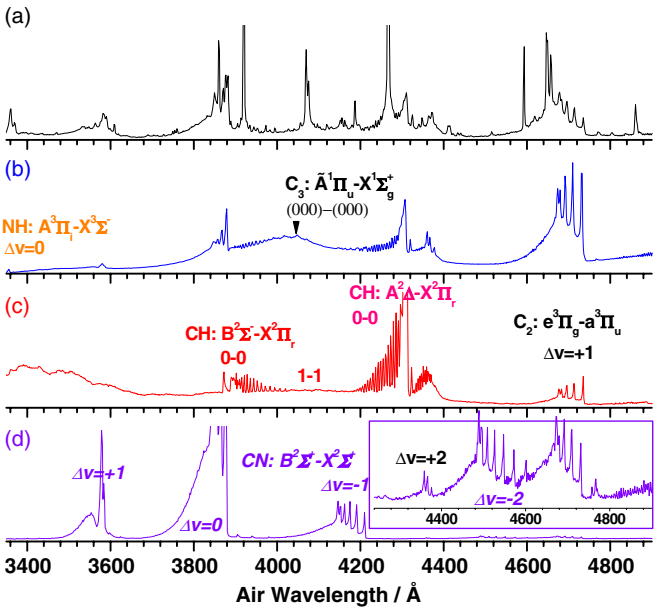

Figure 3. Low-resolution emission spectra from: (a) PLA of carbon at an air pressure of 4 Pa, excited by the 9P(28) line at 1039.36 $\mathrm{cm^{-1}}$ of the CO_2 laser; (b) acetylene/oxygen flame; (c) propane–butane/air flame; (d) free-burning carbon arc.

spectra were recorded under similar experimental conditions to low-resolution spectra (air pressure 4 Pa, CO_2 laser excitation line 9P(28) at 9.621 μm and laser intensity 5.36 $\mathrm{GW\,cm^{-2}}$). The relative intensities of the observed emission lines reasonably agree with tabulated values in NIST Atomic Spectral Database [34]. In figures 4(a)–(f) we have indicated in italics the position of the band heads v'–v'' of the violet system of CN, and in regular typeface the bands of the other molecular systems. In figures 4(a)–(f), a rather complex structure is observed, in consequence of the overlapping between rotational lines of different molecular band systems. Figure 4(a) displays the overlapping between CH(C–X; $\Delta v = 0$ sequence), CN(B–X; $\Delta v = 3$ sequence) and OH(A–X; $\Delta v = 0$ sequence). The relative position of the main branches for the OH(A–X) 0–0 band is indicated. In figure 4(b), the high intensity of the 0–0 band for NH(A–X) is observed. This fact is in agreement with the high Franck–Condon factor ($q_{00} = 0.9998$) for this transition. In figure 4(c) a partial overlapping among CN(B–X; $\Delta v = 1$) and C_2(C–A; $\Delta v = 1$) is observed. This spectrum clearly shows the reversal of the bands from $v'' = 5$, which is due to the overlap between high vibrational quantum number bands with low vibrational quantum number bands. So, the first vibrational bands (1–0, 2–1, 3–2, 4–3 and 5–4) are shaded to the violet and after reversal (6–5, 7–6, ...) are shaded to the red. Figure 4(d) shows a portion of the rotational lines for the CH(B–X) 0–0 band with several single ionized carbon lines. A coincidence in the position among the CN(B–X) 4–4 and C_2(C–A) 0–0 band heads is observed. In the spectrum of figure 4(e) the CN(B–X) $\Delta v = -1$ sequence, CH(A–X) 0–0 band and C_2(d–a) $\Delta v = 2$ sequence were identified. Also, several C^+, C^{2+}, and atomic hydrogen lines are observed. Finally, figure 4(f) displays the rotational structure of the C_2(d–a) 0–1, 1–2 and 2–3 bands. The spectral features clearly show

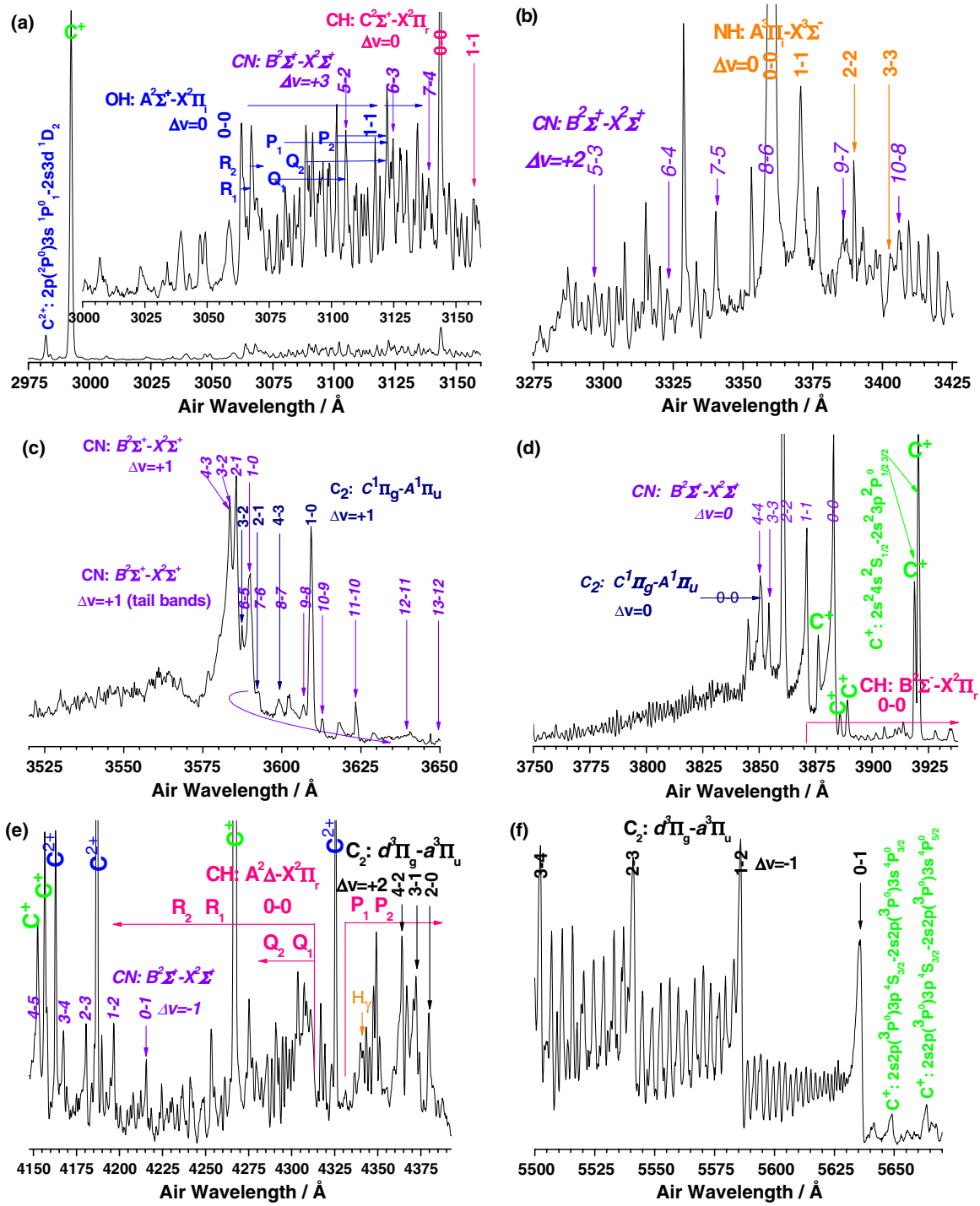

Figure 4. (*a*)–(*f*) Measured high-resolution PLA of carbon emission spectra observed in different regions at an air pressure of 4 Pa, excited by the 9P(28) line of the CO_2 laser with a laser intensity of 5.36 GW cm^{-2}, and assignment of some atomic lines and molecular band heads.

the complexity of the relaxation process and bring out the possibility of cascading processes.

3.2. Plasma excitation temperature measurements

The excitation temperature T_{exc} was calculated according to the Boltzmann equation under the assumption of local thermodynamic equilibrium (LTE). In LTE plasmas, a single temperature characterizes all internal energy modes (electronic, vibrational and rotational). This temperature can be determined from the absolute intensity of any atomic or molecular feature or from Boltzmann plots of vibrational or rotational population distributions. The significance of this temperature depends on the degree of equilibrium within the plasma. For an optically thin plasma, the conditions satisfying this assumption of LTE require that the radiative population rates are negligible compared with the collisional population rates. This essentially implies that an excited state must have a higher probability of de-excitation by collision than by spontaneous emission. For plasma in LTE, any point can

be described by its local values of temperature, density and chemical composition. Usually LTE is established among all the species in the plasma beyond ∼1 μs delay time from the plasma start. For laser fluences around 10 J cm^{-2} the laser-induced plume, after ∼1 μs, essentially contains only neutral atomic and molecular species, and electron density is expected to be very low. However, at higher laser fluences as used in this work (see table 1), in proximity to the carbon target surface, the plasma is formed by neutral atomic, highly ionized carbon and molecular species (see figures 2 and 4). The excitation temperature was calculated from the relative intensities of some C^+ atomic lines (250–470 nm spectral region) from the slope of the Bolztmann plot $\ln[I_{ki} \cdot \lambda_{ki}/g_k \cdot A_{ki}]$ versus E_k/k_B (figure 5):

$$\ln\left[\frac{I_{ki} \cdot \lambda_{ki}}{g_k \cdot A_{ki}}\right] = C_1 - \frac{E_k}{k_B \cdot T_{exc}}, \qquad (6)$$

where I_{ki} is the emissivity (W m^{-3} sr^{-1}) of the emitted $k \rightarrow i$ spectral line, λ_{ki} is the wavelength, $g_k = 2J_k + 1$ is the statistical weight, A_{ki} is the Einstein transition probability of spontaneous emission, E_k/k_B is the normalized energy of the upper electronic level (k_B is Boltzmann's constant) and $C_1 = \ln(hcN_k/4\pi Q(T))$ ($Q(T)$ is the partition function). The values of λ_{ki}, g_k, A_{ki} and E_k for C^+ selected atomic lines were obtained from the NIST Atomic Spectral Database. The estimation of excitation temperature has been carried out from the PLA spectrum at a laser irradiance of 1.00 GW cm^{-2} (P_{air} = 4 Pa). The estimated excitation temperature was T_{exc} = 23 000 ± 1900 K (figure 5). These spectral lines were chosen based on their relative strengths, accuracies and transition probabilities. The relevant spectroscopic parameters for the C^+ transitions have been listed in table 2.

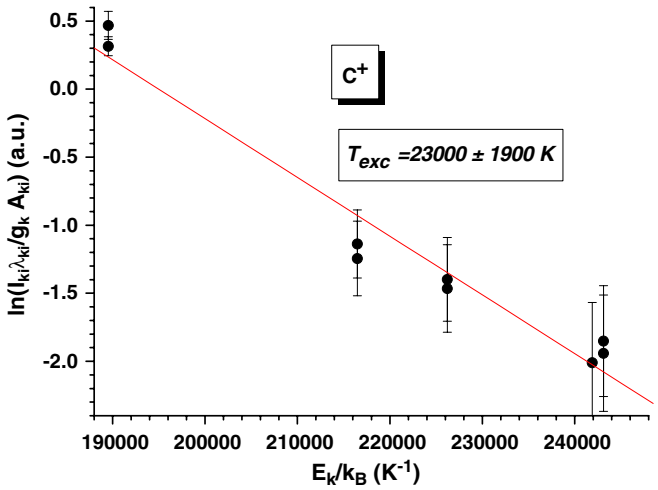

Figure 5. Linear Boltzmann plot for several C^+ transition lines used to calculate plasma temperature, T_{exc}. Plot also shows linear fit to the data with a regression coefficient of $R^2 \sim 0.98$.

3.3. Ionization degree of the plasma

As the CO_2 laser beam is focused on the graphite surface, the carbon material absorbs the laser energy to melt, vaporize and excite the target material. The carbon vapour absorbs more energy and forms high temperature plasma near the surface. The plasma expands into the low-vacuum atmosphere (N_2, O_2, H_2O, etc) and transfers its energy to it. If the pressure around the target is greater than ∼1000 Pa, the breakdown of the air takes place in a significant way. Neutral, single and highly ionized carbon emission lines are found close to the target graphite surface. The carbon clusters and the molecules of the atmosphere obtain an energy that exceeds the binding energy. In these conditions the plasma becomes a mixture of electrons, positive ions such as C^+, C^{2+}, C^{3+}, C^{3+}, C^{4+}, neutral atoms such as C, N, O and H, and molecules such as C_2, CN, CH, NH and OH in excited electronic states. In plasma there is a continuous transition from gases with neutral atoms to a state with ionized atoms, which is determined by an ionization equation. The transition between a gas and a plasma is essentially a chemical equilibrium, which shifts from the gas to the plasma side with increasing temperature. Let us consider the first three different ionization equilibria of carbon:

$$C(2s^2 2p^2\ ^3P_o) \leftrightarrow C^+(2s^2 2p\ ^2P^o_{1/2}) + e + IP(C\text{-}I),$$

$$C^+(2s^2 2p\ ^2P^o_{1/2}) \leftrightarrow C^{2+}(2s^2\ ^1S_0) + e + IP(C\text{-}II),$$

$$C^{2+}(2s^2\ ^1S_0) \leftrightarrow C^{3+}(2s^1\ ^2S_{1/2}) + e + IP(C\text{-}III),$$

where the first three ionization potentials (IPs) for carbon are $E_i^{C\text{-}I}$ = IP(C-I) = 11.2603 eV, $E_i^{C\text{-}II}$ = IP(C-II) = 24.3833 eV and $E_i^{C\text{-}III}$ = IP(C-III) = 47.8878 eV [40]. For each ionization equilibrium, the LTE between ionization and

Table 2. List of C^+ transition lines and their spectral database (NIST Atomic Spectra Database, 2006) used for plasma temperature calculation.

Transition array	Air λ (Å)	g_i	g_k	A_{ki} (s^{-1})	E_i (cm^{-1})	E_k (cm^{-1})	Rel. Int. (arb. uni.)
$2s2p^2\ ^2P_{1/2}$–$2p^3\ ^2D^o_{3/2}$	2509.12	2	4	4.53×10^7	110 624.17	150 466.69	20 800
$2s2p^2\ ^2P_{3/2}$–$2p^3\ ^2D^o_{5/2}$	2512.06	4	6	5.42×10^7	110 665.56	150 461.58	41 500
$2s^23p\ ^2P^o_{1/2}$–$2s^2\ 4d\ ^2D_{3/2}$	2746.49	2	4	4.36×10^7	131 724.37	168 123.74	8500
$2s2p^2\ ^2S_{1/2}$–$2s^23p\ ^2P^o_{3/2}$	2836.71	2	4	3.98×10^7	96 493.74	131 735.52	76 900
$2s2p^2\ ^2S_{1/2}$–$2s^23p\ ^2P^o_{1/2}$	2837.60	2	2	3.97×10^7	96 493.74	131 724.37	44 700
$2s^23p\ ^2P^o_{1/2}$–$2s^2\ 4s\ ^2S_{1/2}$	3918.98	2	2	6.36×10^7	131 724.37	157 234.07	7500
$2s^23p\ ^2P^o_{3/2}$–$2s^2\ 4s\ ^2S_{1/2}$	3920.69	4	2	1.27×10^8	131 735.52	157 234.07	16 000
$2s^23d\ ^2D_{3/2}$–$2s^2\ 4f\ ^2F^o_{5/2}$	4267.00	4	6	2.23×10^8	145 549.27	168 978.34	45 000
$2s^23d\ ^2D_{5/2}$–$2s^2\ 4f\ ^2F^o_{7/2}$	4267.26	6	8	2.38×10^8	145 550.70	168 978.34	70 000

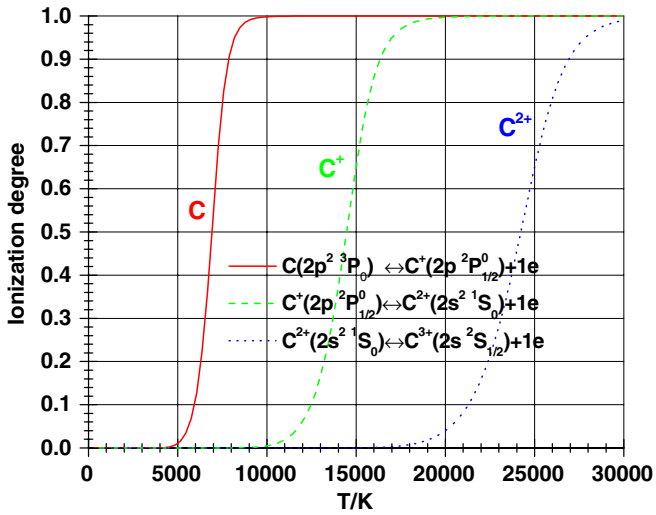

Figure 6. Temperature dependence of the ionization degree $N_i/(N_0 + N_i)$ of carbon C, carbon singly ionized C^+ and carbon doubly ionized C^{2+} at a constant pressure of 4 Pa.

recombination reactions at temperature T is described by the Saha equation

$$\frac{n_e \cdot N_i}{N_0} = \frac{g_e \cdot g_i}{g_0} \frac{(2\pi m_e k_B T)^{3/2}}{h^3} e^{-E_i/k_B T}, \quad (7)$$

where $n_e = N_i$ are the electron and ion densities in the different ionization equilibria in the second member of ionization equilibria, N_0 the density of the carbon or ions in the first member of ionization equilibria, h Planck's constant, k_B Boltzmann's constant, m_e the electron mass and g_e, g_i and g_0 the statistical weights of the electrons ($g_e = 2$), C^+ ions ($g_i = 2$), C^{2+} ions ($g_i = 1$), C^{3+} ions ($g_i = 2$) and C neutrals ($g_0 = 1$). The Saha equation reads

$$\frac{n_e \cdot N_i}{N_0} = C T^{3/2} e^{-E_i/k_B T}, \quad (8)$$

with $C = 9.6587 \times 10^{21}$, 2.4147×10^{21} and $9.6587 \times 10^{21}\,K^{-2/3}\,m^{-3}$ for the first three ionization equilibria of carbon, respectively, and T is in K. Figure 6 shows the ionization degree $N_i/(N_0 + N_i)$ of C, C^+ and C^{2+}, plotted as a function of the gas temperature T at a constant total pressure $P = (N_0 + n_e + N_i)k_B T$ of 4 Pa. The graph shows that carbon is already fully ionized at thermal energies well below the first ionization energy of 11.2603 eV (equivalent to 130 670 K). If we consider a temperature of 23 000 K, the ionization degrees of C, C^+ and C^{2+} obtained by means of the Saha equation (8) are 0.999, 0.999 and 0.28, respectively. These so high values of the ionization degrees justify the observed emission spectra. Keeping in mind these results, the temperature obtained from the relative intensity of C^+ lines was chosen as the first approximation for the excitation temperature.

3.4. Electron number density

The evolution of the laser-plasma can be divided into several transient phases. The initial plasma (~0–100 ns) is characterized by high electron and ion densities (10^{17}–$10^{20}\,cm^{-3}$) and temperatures around 30 000 K. Of course, the density gradient of the plasma is highest in the earliest time of plume expansion. The emission spectrum for the early stage of the plasma is characterized by a continuum background emission mainly due to bremsstrahlung and recombination processes of electrons with ions in the plasma. Structured emission spectra from atomic and ionized species and molecular bands can be found after about 300 ns delay. Observed spectral lines are always broadened, partly due to the finite resolution of the spectrometer and partly to intrinsic physical causes. The principal physical causes of spectral line broadening are the Doppler, resonance pressure and Stark broadening. The Doppler broadening is due to the thermal motion of the emitting atoms or ions. For a Maxwellian velocity distribution the line shape is Gaussian, and the FWHM may be estimated as (Å): $\Delta\lambda^D_{FWHM} = 7.16 \times 10^{-7} \cdot \lambda \cdot \sqrt{T/M}$, λ being the wavelength in Å, T the temperature of the emitters in K and M the atomic mass in amu. In our experiments, for C^+ lines, the Doppler line widths are 0.08–0.13 Å at 23 000 K. Stark line broadening from collisions of charged species is the primary mechanism influencing the emission spectra in these experiments. The FWHM of the Stark broadened lines is related to the electron number density n_e (cm^{-3}) by [41]

$$\Delta\lambda^S_{FWHM} = 2W\left(\frac{n_e}{10^{16}}\right) + 3.5A\left(\frac{n_e}{10^{16}}\right)^{1/4} \times \left(1 - BN_D^{-1/3}\right)W\left(\frac{n_e}{10^{16}}\right), \quad (9)$$

where W is the electron impact parameter or half-width, A is the ion impact parameter, both in Å, B is a coefficient equal to 1.2 or 0.75 for ionic or neutral lines, respectively, and N_D is the number of particles in the Debye sphere

$$N_D = 1.72 \times 10^9 \frac{T^{3/2}}{n_e^{1/2}}. \quad (10)$$

The electron and the ion impact parameters are functions of temperature. The first term on the right side of equation (9) refers to the broadening due to the electron contribution, whereas the second one is the ion broadening. Since for PLA conditions Stark broadening is predominantly by electron impact, the ion correction factor can safely be neglected, and equation (9) becomes

$$\Delta\lambda^{S}_{\mathrm{FWHM}} = 2W\left(\frac{n_{\mathrm{e}}}{10^{16}}\right). \tag{11}$$

The choice of plasma emission for n_{e} measurements is made to ensure that the C^+ spectral lines are sensitive enough to the Stark effect and do not suffer from interference by other species. In our case, the estimation of electron density n_{e} has been carried out by measuring the broadening of the spectral profiles of isolated lines of C^+ (2174, 2747, 2837, 2993, 3877, 3920, 4267 and 5890 Å) from the high-resolution spectra. The electron number densities of the laser-induced plasma were determined at a laser power density of $I_{\mathrm{W}} = 1\,\mathrm{GW\,cm^{-2}}$ and air pressure of 4 Pa. A Lorentz function was used to fit the spectra. In order to extract the Stark broadening from the total experimentally measured line broadening, we have to previously deconvolute the different effects that contribute to the broadening of the spectral line: the instrumental, Doppler and Stark broadenings. Values of the electron impact half-width W were taken from the extensive tables given by Griem [41]. Determination of electron density n_{e} by this method is independent of any assumptions regarding LTE conditions. Electron densities in the range $(0.69–5.6) \times 10^{16}\,\mathrm{cm^{-3}}$, with an estimated uncertainty of 10%, were determined from the Stark broadening data of several singly ionized carbon lines. The validity criteria for LTE and consequently criteria for the application of the different spectroscopic methods are extensively discussed in the literature [42,43]. For the LTE, the excited states have to be populated through collisions. Using the McWhirter's criterion [44] to check the condition for the validity of the LTE, we find that the electron number density satisfies

$$n_{\mathrm{e}} \geqslant 1.6 \times 10^{12} T^{1/2} (\Delta E)^3. \tag{12}$$

Here, n_{e} ($\mathrm{cm^{-3}}$) is the electron density, T (K) is the plasma temperature and ΔE (eV) is the difference in the energies between the upper and the lower states of all the C^+ investigated transitions. At the evaluated temperature of $23\,000 \pm 1900$ K, equation (12) yields $n_{\mathrm{e}} \approx (0.39–2.2) \times 10^{16}\,\mathrm{cm^{-3}}$. These electron densities are close to the measured values. Based on these calculations, it is difficult to tell whether the plasma is in LTE or not. A possible reason for non-thermal equilibrium could be the large integration time used in the experiments. At these later times, the collisions among the species decrease due to drop in densities.

3.5. Effect of laser irradiance

Laser–sample and laser–plasma interactions are strongly dependent on the laser beam irradiance on the target. To see the effect of laser irradiance the measurements were also carried out at different laser fluences. Optical emission spectra of the carbon plasma plume in low vacuum (~4 Pa) as a function of the laser intensity are shown in figures 7(*a*) and (*b*). As indicated above, these spectra were recorded at a constant distance of 1.5 cm from the target surface along the plasma expansion direction and after the incidence of only one pulse of the CO_2 laser. The data were measured at a delay of 20 ms. As we have already indicated above, the laser pulse consisted of a 64 ns spike carrying ~90% of the energy and a 3 μs lasting tail. For example, for a laser pulse energy of 2685 mJ, the laser power or radiant pulse energy per time (equation (1)) of the spike is 37.7 and 0.089 MW for the tail. Considering the fast plume expansion, the major part of the tail of the laser pulse will reach the target. Using this laser pulse one can expect that the leading edge of the 64 ns pulse will create plasma above the target and the 3 μs lasting tail will be used for heating the plasma, without producing further ablation. An increase in atomic and molecular emission intensity with increasing laser fluence was observed. Figure 8 shows the emission intensity change of C(247.856 nm), C^+(251.206 nm), C^{2+}(269.775 nm), C^{3+}(252.998 nm), C^{4+}(227.792 nm), OH 0–0 band head (306.35 nm) and NH 1–0 band head (336.00 nm) as a function of the carbon dioxide laser fluence. The C^{3+}, C^+ and C emission intensity increases drastically with the laser fluence. Beyond ~100 J $\mathrm{cm^{-2}}$, a sharp increase in atomic

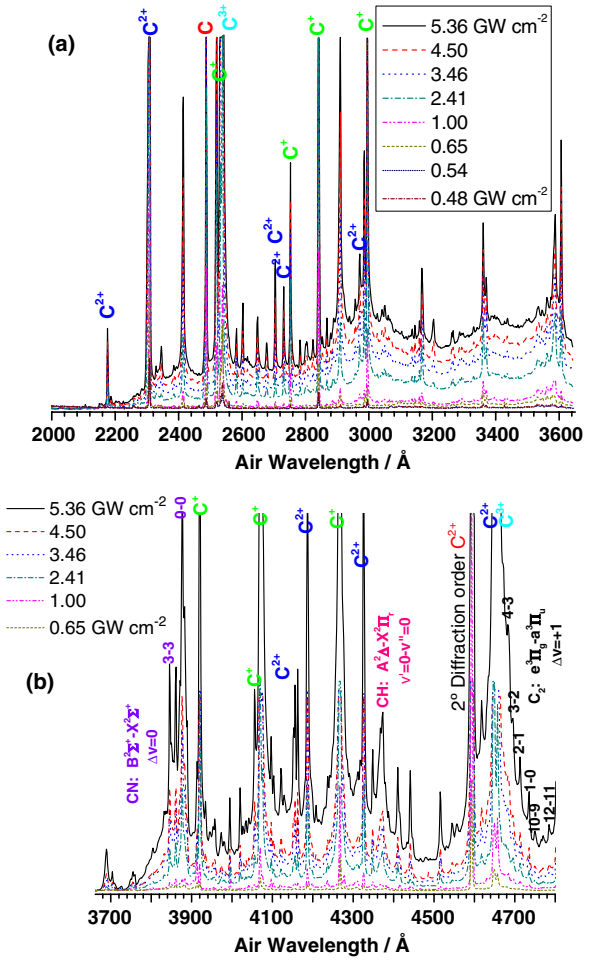

Figure 7. Low-resolution PLA of carbon emission spectrum observed in the (*a*) 2000–3640 Å and (*b*) 3660–4800 Å regions, at an air pressure of 4 Pa, excited by the 9P(28) line at 1039.36 $\mathrm{cm^{-1}}$ of the CO_2 laser, as a function of the laser power density.

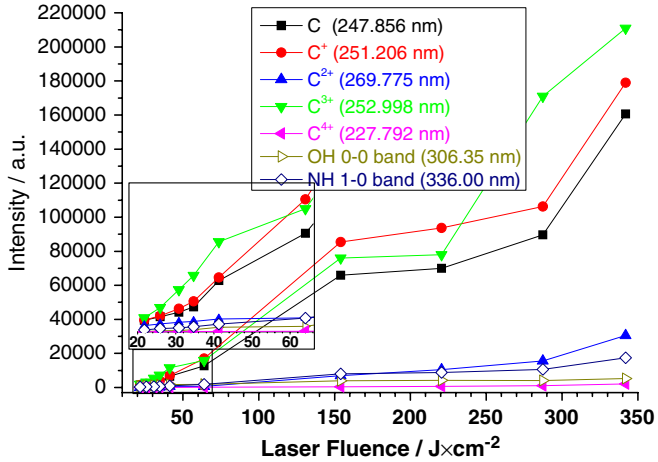

Figure 8. Emission intensity change of C(247.856 nm), C^{+}(251.206 nm), C^{2+}(269.775 nm), C^{3+}(252.998 nm), C^{4+}(227.792 nm), OH 0–0 band head (306.35 nm), and NH 1–0 band head (336.00 nm) as a function of the carbon dioxide laser fluence.

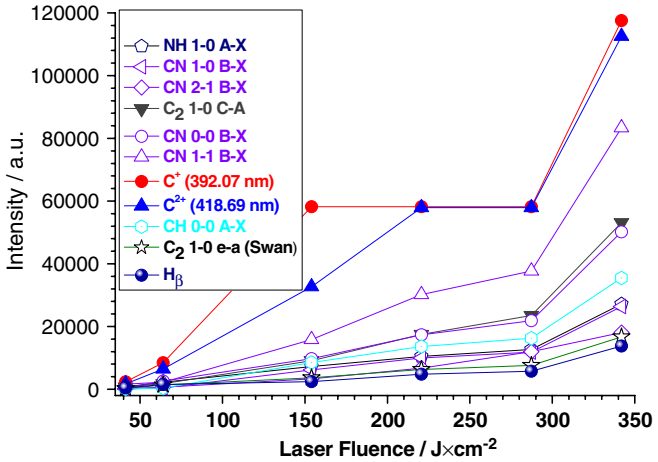

Figure 9. Emission intensity change of C^{+}(392.07 nm), C^{2+}(418.69 nm), NH 1–0 band head of the $A\,^3\Pi$–$X\,^3\Sigma^-$ system, CN 1–0, 2–1, 0–0, 1–1 band heads of the $B\,^2\Sigma^+$–$X\,^2\Sigma^+$ violet system, C_2 1–0 band head of the $C\,^1\Pi_g$–$A\,^1\Pi_u$, CH 0–0 band head of the $A\,^2\Delta$–$X\,^2\Pi$, C_2 1–0 band head of the Swan system $e\,^3\Pi_g$–$A\,^3\Pi_u$, and H_β line as a function of the carbon dioxide laser fluence.

(especially for C^{3+}, C^{+} and C) and molecular line intensities was observed. The C^{2+}, C^{4+}, OH 0–0 band head and the NH 1–0 band head emission intensity increases lightly with the laser fluence. These measurements were carried out from the UV spectra of figure 7(*a*) in the spectral region between 200 and 360 nm. Figure 9 shows the emission intensity change of C^{+}(392.07 nm), C^{2+}(418.69 nm), NH 1–0 band head of the A–X system, CN 1–0, 2–1, 0–0, 1–1 band heads of the B–X violet system, C_2 1–0 band head of the $C\,^1\Pi_g$–$A\,^1\Pi_u$ Deslandres–d'Azambuja system, CH 0–0 band head of the A–X system, C_2 1–0 band head of the e–a Swan system and the H_β line as a function of the laser fluence. An increase in atomic and molecular emission intensity with increasing laser fluence was observed. Also the background increases with the laser power. At higher laser fluences (154–342 J cm^{-2}), the spectral lines and the molecular bands are considerably more broadened than at lower fluences as a result of the high pressure associated with the plasma. It is assumed that at higher laser fluence the PLA plasma is more energetic and more ionized so that the surrounding air can confine the plasma better; the plasma also cools down more rapidly due to the confinement.

3.6. The calculation of the vibrational temperature

The detection of the C_2(d–a) Swan and the CN(B–X) bands is of particular interest since it provides an estimation of the plasma plume temperature by a different method that was employed in section 3.2. The emission intensities of the C_2 Swan $\Delta v = -1$ and CN $\Delta v = 0$ band sequences were analysed in order to calculate the molecular vibrational temperature T_{vib}. For a plasma in LTE, the intensity of an individual vibrational v'–v'' band $I_{v'-v''}$ is given by

$$\ln\left(\frac{I_{v'-v''}\cdot\lambda^4_{v'-v''}}{q_{v'-v''}}\right) = A - \frac{G(v')hc}{k_{\mathrm{B}}\cdot T_{\mathrm{vib}}}, \qquad (13)$$

where A is a constant, $\lambda_{v'-v''}$ is the wavelength corresponding to the band head, $q_{v'-v''} = |\int_0^\infty \Psi_{v'}(R)\Psi_{v''}(R)\,\mathrm{d}R|^2$ is the Franck–Condon factor and $G(v')hc/k_{\mathrm{B}}$ is the normalized energy of the upper vibrational level. A line fit to $\ln(I_{v'-v''}\cdot\lambda^4_{v'-v''}/q_{v'-v''})$ as a function of the upper normalized electronic–vibrational energies has a slope equal to $-1/T_{\mathrm{vib}}$. Two Boltzmann plots of the band intensities against the vibrational energy at the laser irradiance 4.5 GW cm^{-2} are given in figure 10 along with the corresponding Franck–Condon factors. For C_2 and CN the estimated vibrational temperatures were $T_{\mathrm{vib}} = 18\,800 \pm 860$ K (figure 10(*a*)) and $21\,400 \pm 900$ K (figure 10(*b*)), respectively. These values are slightly inferior to those obtained in section 3.2. This fact indicates that, at 4 Pa, although the system cannot be under LTE condition, it would be very near it. Habitually, when one works at higher pressures, LTE condition is guaranteed. Figure 11 shows the variation of vibrational temperature at 4 Pa of air pressure with laser fluence. The vibrational temperature is the maximum at a most efficient laser fluence of 287 J cm^{-2}. These results are consistent with earlier reports on vibrational temperature by different authors [11, 13, 18, 20, 22, 28, 30]. It has been observed [7] that the degree of the diamond-like character in DLC films varies due to different temperatures in the laser-induced plasma. This can be due to the fact that the sp^3 fraction in deposited films increases when the energy of the particles increases. The deposition of DLC films at this optimum energy may help in optimizing the film quality.

3.7. Effect of ambient pressure on the plasma

The emission characteristics of the laser-induced plasma are influenced to a large extent by the nature and composition of the surrounding atmosphere. The pressure of the air ambient atmosphere is one of the controlling parameters of the plasma characteristics, as well as the factors related to the laser energy absorption. The presence of air during the ablation process has dramatic consequences on the expansion dynamics. An interesting observation was the effect of the air pressure,

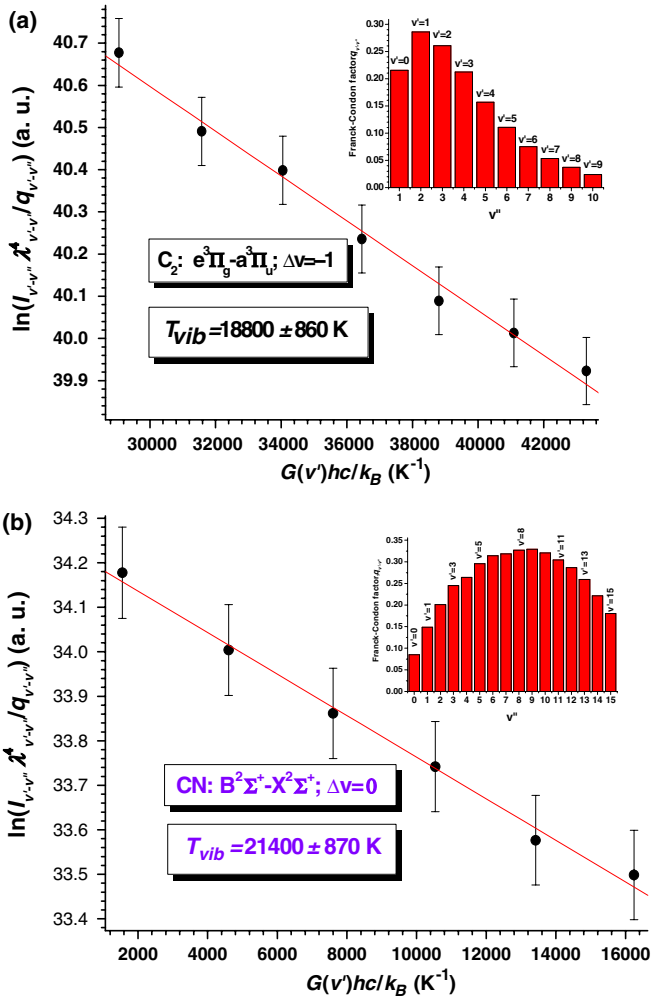

Figure 10. (*a*) Linear Boltzmann plot of the C_2 Swan $\Delta v = -1$ band sequence intensity versus the normalized energy of the upper vibrational level; (*b*) Linear Boltzmann plot of the CN violet $\Delta v = 0$ band sequence intensity versus the normalized energy of the upper vibrational level; Experimental conditions: laser power density of 4.5 GW cm^{-2} and vacuum pressure 4 Pa. Plots also show linear fits to the data and the corresponding Franck–Condon factors.

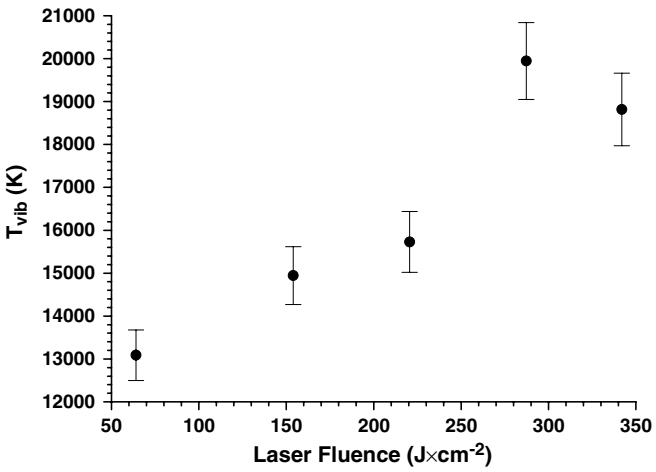

Figure 11. The vibrational temperature T_{vib} calculated from the C_2 Swan $\Delta v = -1$ sequence bands as a function of the CO_2 laser fluence.

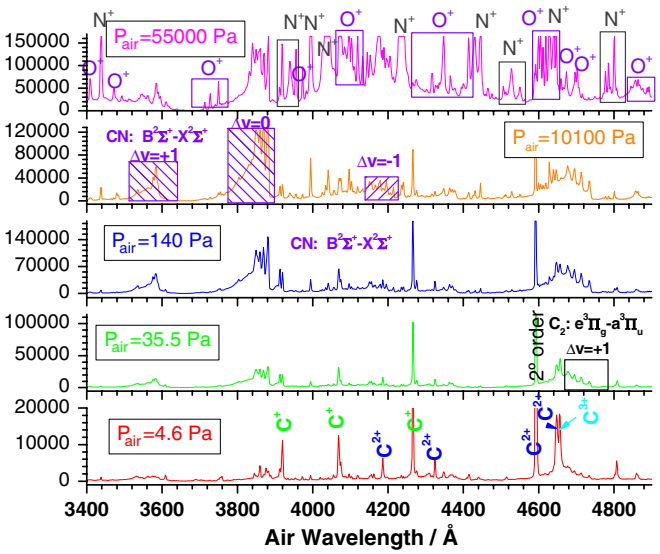

Figure 12. Low-resolution PLA of carbon OES observed in the 3400–4880 Å region at various air pressures. The plasma plumes were induced by the TEA-CO_2 (9P(28) line at 1039.36 cm^{-1}) laser power density of 1.00 GW cm^{-2}.

studied in the range 4.6–63 500 Pa. Figures 12 and 13 show typical OES from a carbon plasma plume at different air pressures. These plasma plumes were generated by the CO_2 laser intensity of 1.00 GW cm^{-2}. In general, the spectra of the PLA plume at low pressures ($P < 1500$ Pa) are dominated by emission of electronic relaxation of excited atomic C, N, H, O, ionic fragments C^+, C^{2+} C^{3+} and C^{4+}, and molecular features of $C_2(E–A)$, $C_2(D–X)$, $C_2(d–a)$, $C_2(D–X)$, $C_2(e–a)$, $C_2(C–A)$, $C_2(A–X)$, CN($D–A$), CN($B–X$), CN($A–X$), OH($A–X$), NH($A–X$), CH($C–X$), CH($B–X$) and CH($A–X$). The spectra of the PLA plume at high pressures ($P > 10\,000$ Pa) are dominated by emission of electronic relaxation of excited atomic N, O, H, ionic fragments N^+ and O^+, and molecular features of CN($B–X$) and CN($A–X$). The intensities of the C_2 1–0 band head of the $C\,^1\Pi_g–A\,^1\Pi_u$ (3607 Å), C_2 1–0 band head of the $D\,^1\Sigma_u^+–X\,^1\Sigma_g^+$ (4737 Å), CN 1–0 and 0–0 band heads of the $B\,^2\Sigma^+–X\,^2\Sigma^+$ violet system, CH 0–0 band head of the $A\,^2\Delta–X\,^2\Pi$ (4307 Å), C^+(3919 Å), C^+(4267 Å), C^{2+}(4593 Å), C^{3+}(4657 Å), and H_β spectral lines increase with increasing pressure, reach a maximum at about 200 Pa, and then decrease with higher pressures. Similar results were reported in the literature [45, 46]. Figure 14 shows the evolution of the emission intensity of the C_2 1–0 band head of the $C\,^1\Pi_g–A\,^1\Pi_u$ (3607 Å), C_2 1–0 band head of the $D\,^1\Sigma_u^+–X\,^1\Sigma_g^+$ (4737 Å), CN 1–0 and 0–0 band heads of the $B\,^2\Sigma^+–X\,^2\Sigma^+$ violet system, CH 0–0 band head of the $A\,^2\Delta–X\,^2\Pi$ (4307 Å), N^+(3437 Å), O^+(3410 Å), C^+(3919 Å), C^+(4267 Å), C^{2+}(4593 Å), C^{3+}(4657 Å) and H_β atomic lines as a function of air pressure. From figure 14, the intensity of the C^{2+}(4593 Å), C^+(4267 Å) and C^{3+}(4657 Å) spectral lines is found to be more sensitive to the pressure than the CH 0–0 band head of the $A–X$ (4307 Å), C^+(3919 Å) and H_β atomic lines. The lines N^+(3437 Å) and O^+(3410 Å) produced in the breakdown of the air are not observed in the PLA of carbon at low air pressures. The intensity of CN ($\Delta v = 0$ sequence) increases

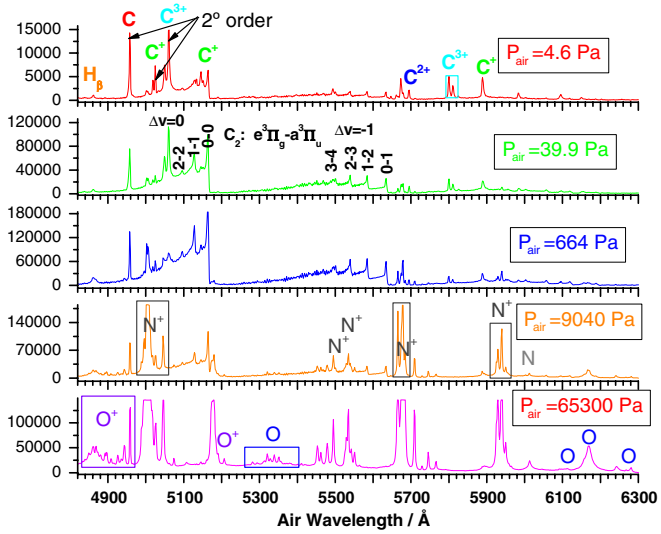

Figure 13. Low-resolution PLA of carbon OES observed in the 4800–6300 Å region at various air pressures. The plasma plumes were induced by the TEA-CO_2 (9P(28) line at 1039.36 cm^{-1}) laser power density of 1.00 GW cm^{-2}.

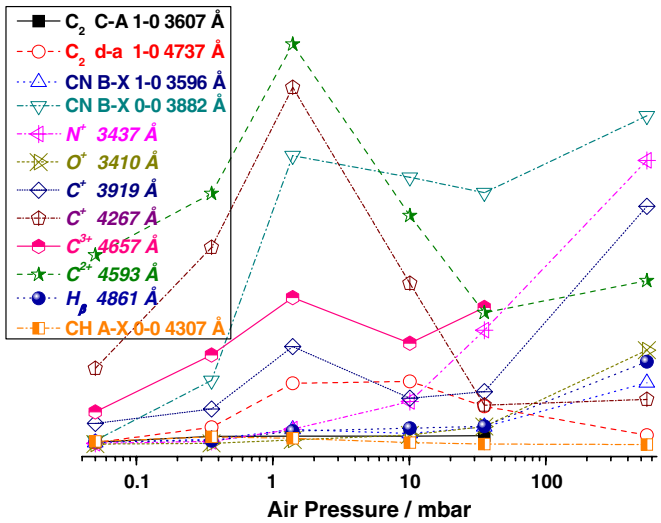

Figure 14. Emission intensity change of C_2 1–0 band head of the $C\,^1\Pi_g$–$A\,^1\Pi_u$ (3607 Å), C_2 1–0 band head of the $D\,^1\Sigma_u^+$–$X\,^1\Sigma_u^+$ (4737 Å), CN 1–0 and 0–0 band heads of the $B\,^2\Sigma^+$–$X\,^2\Sigma^+$ violet system, CH 0–0 band head of the $A\,^2\Delta$–$X\,^2\Pi$ (4307 Å), N^+ (3437 Å), O^+ (3410 Å), C^+(3919 Å), C^+(4267 Å), C^{2+}(4593 Å), C^{3+}(4657 Å) and H_β lines as a function of the air pressure around the carbon target.

with increasing air pressure, reaches a maximum at about 200 Pa and then stays constant as the pressure is increased further. Beyond 200 Pa (see figure 14), a decrease in the time-integrated emission intensities of C^+, C^{2+}, C^{3+}, CN, C_2, CH, NH and H was found. However, an increase in the emission intensities of the N^+ and O^+ lines was observed. We suggest that these effects are related to shielding by the air plasma, where a part of the laser energy is absorbed by the air plasma during its expansion. This results in a reduction of the atomic and ionic emission intensity of species formed from the carbon target. At low pressures ($P < 200$ Pa), the C, C^+, C^{2+}, C^{3+} and CN, C_2, CH, NH emissions are produced nearer to the carbon target than the N^+ and O^+ emissions produced nearer to the air plasma position. In general, the air ambient gas will confine the plasma near the target (produced mainly by C, C^+, C^{2+}, C^{3+} and CN, C_2, CH) and prevent the electrons and species produced near the target from escaping quickly from the laser focal volume (observation region). Therefore, the emission intensity increases with increasing pressure. However, at higher pressures (more than 200 Pa in our case), the ambient gas will hinder the plasma from penetrating the atmosphere and predictably cause a higher plasma temperature. The emission intensity of H, C, C^+, C^{2+}, C^{3+} and CN, C_2, CH decreases because of the fact that the laser energy is absorbed by air, producing air breakdown and increasing the N, O, N^+ and O^+ emission intensity, in agreement with our observation in figure 13. At lower air pressures, the absence of the shielding air plasma results in a strong increase in the intensity of the C, C^+, C^{2+}, C^{3+} emission from the carbon target plasma. At such lower air pressures the relative contribution of the N^+, O and O^+ emission diminishes, and the emission from the carbon surface component becomes dominant.

4. Conclusions

The PLA generated by CO_2 laser pulses in graphite in a low-vacuum atmosphere has been investigated by means of OES. The emission observed in the plasma region is mainly due to the relaxation of excited atomic C, N, O and H, ionic fragments C^+, C^{2+}, C^{3+}, and C^{4+}, and molecular bands of $C_2(E–A)$, $C_2(d–a)$, CN($D–A$), CN($B–X$), CN($A–X$), $C_2(D–X)$, $C_2(e–a)$, $C_2(C–A)$, OH($A–X$), NH($A–X$), CH($C–X$), CH($B–X$) and CH($A–X$). An excitation temperature around 23 000 K and electron densities in the range (0.6–5.6) $\times$ 10^{16} cm^{-3} were estimated by means of C^+ lines. Estimates of vibrational temperatures of C_2 electronically excited species under various laser power density conditions are made. The characteristics of the spectral emission intensities from different species have been investigated as functions of the ambient pressure and laser irradiance.

Acknowledgments

This work was partially supported by the Spanish MEC Project CTQ2007-60177/BQU. It is a pleasure to acknowledge the excellent technical support of A Magro.

References

[1] Okano K, Koizumi S, Silva S R P and Amaratunga G A J 1996 *Nature* **381** 140
[2] Chuang F Y, Sun C Y, Chen T T and Lin I N 1996 *Appl. Phys. Lett.* **69** 3504
[3] Fan S, Chapline M G, Franklin N R, Tombler T W, Cassell A M and Dai H 1999 *Science* **283** 512
[4] Yoshimoto M *et al* 1999 *Nature* **399** 340
[5] Matsumoto S 2000 *Thin Solid Films* **368** 231
[6] Chen X H *et al* 2001 *J. Cryst. Growth* **222** 163
[7] Pappas D L *et al* 1992 *J. Appl. Phys.* **71** 5675
[8] Rohlfing E A 1988 *J. Chem. Phys.* **89** 6103
[9] Chen X and Mazumder J 1990 *Appl. Phys. Lett.* **57** 2178
[10] Iida Y and Yeung E 1994 *Appl. Spectrosc.* **48** 945

[11] Dwivedi R K and Thareja R K 1995 *Phys. Rev.* B **51** 7160
[12] Tasaka Y, Tanaka M and Usami S 1995 *Japan. J. Appl. Phys.* **34** 1673
[13] Harilal S S, Issac R C, Bindhu C V, Nampoori V P N and Vallabhan C P G 1996 *J. Appl. Phys.* **80** 3561
[14] Demyanenco A V, Letokhov V S, Puretskii A A and Ryabov E A 1997 *Quantum Electron.* **27** 983
[15] Demyanenco A V, Letokhov V S, Puretskii A A and Ryabov E A 1998 *Quantum Electron.* **28** 33
[16] Aoqui S, Ikegami T, Yamagata Y and Ebihara K 1998 *Thin Solid Films* **316** 40
[17] Vivieny C, Hermanny Perronez J A, Boulmer-Leborgney C and Luchesz A 1998 *J. Phys. D: Appl. Phys.* **31** 1263
[18] Wee S and Park S M 1999 *Opt. Commun.* **165** 199
[19] Yamagata Y, Sharma A, Narayan J, Mayo R M, Newman J W and Ebihara K 1999 *J. Appl. Phys.* **86** 4154
[20] Yamagata Y, Sharma A, Narayan J, Mayo R M and Newman J W 2000 *J. Appl. Phys.* **88** 6861
[21] Harilal S S 2001 *Appl. Surf. Sci.* **172** 103
[22] Acquaviva S and Giorgi M L 2002 *J. Phys. B: At. Mol. Opt. Phys.* **35** 795
[23] Abd S, Physelli-Messaci Kerdja J T, Bendib A and Malek S 2002 *J. Phys. D: Appl. Phys.* **35** 2772
[24] Claeyssens F *et al* 2002 *J. Appl. Phys.* **91** 6162
[25] Saito K, Sakka T and Ogata H 2003 *J. Appl. Phys.* **94** 5530
[26] Zelinger Z, Novotny M, Bulir J, Lancok J, Kubat P and Jelinek M 2003 *Contrib. Plasma Phys.* **43** 426
[27] Saidane K, Razafinimanana M, Lange H, Huczko A, Baltas M, Gleizes A and Meunier J L 2004 *J. Phys. D: Appl. Phys.* **37** 232
[28] Park H S, Nam S H and Park S M 2004 *Bull. Korean Chem. Soc.* **25** 620
[29] Siew W O, Wong K H, Yap S S and Tou T Y 2005 *IEEE Trans. Plasma Sci.* **33** 176
[30] Park H S, Nam S H and Park S M 2005 *J. Appl. Phys.* **97** 113103
[31] Fuge G M, Ashfold M N R and Henley S J 2006 *J. Appl. Phys.* **99** 14039
[32] Camacho J J, Poyato J M L, Díaz L and Santos M 2007 *J. Phys. B: At. Mol. Opt. Phys.* **40** 4573
[33] Camacho J J, Poyato J M L, Díaz L and Santos M 2007 *J. Appl. Phys.* **102** 103302
[34] NIST Atomic Spectra Database online at http://physics.nist.gov/PhysRefData/ASD/index.html
[35] Herzberg G 1950 *Spectra of Diatomic Molecules* (New York: Van Nostrand-Reinhold)
[36] Huber K P and Herzberg G 1979 *Molecular Spectra an Molecular Structure: IV. Constants of Diatomic Molecules* (New York: Van Nostrand-Reinhold)
[37] Gaydon A G 1968 *Dissociation Energies and Spectra of Diatomic Molecules* (London: Chapman and Hall)
[38] Steinfeld J I 1986 *An Introduction to Modern Molecular Spectroscopy* (London: MIT Press)
[39] Bernath P F 1995 *Spectra of Atoms and Molecules* (New York: Oxford University Press)
[40] Martin W C and Zalubas R 1983 *J. Phys. Chem. Ref. Data* **12** 323
[41] Griem H R 1974 *Spectral Line Broadening by Plasmas* (New York: Academic)
[42] Griem H R 1964 *Plasma Spectroscop* (New York: McGraw-Hill)
[43] Griem H R 1997 *Principles of Plasma Spectroscopy* (Cambridge: Cambridge University Press)
[44] McWhirter R W P 1965 *Plasma Diagnostic Techniques* ed R H Huddlestone and S L Leonard (New York: Academic) chapter 5
[45] Kim D E, Yoo K J, Park H K, Oh K J and Kim D W 1997 *Appl. Spectrosc.* **51** 22
[46] Lu Y F, Tao Z B and Hong M H 1999 *Japan. J. Appl. Phys.* **38** 2958